SCIENTIFIC REPORTS

OPEN

SUBJECT AREAS:
ELECTROCHEMISTRY
SYNTHESIS AND PROCESSING

Received
24 October 2013

Accepted
6 January 2014

Published
27 January 2014

Correspondence and requests for materials should be addressed to Y.X.Z. (zhangyuxin@cqu.edu.cn); L.L.Z. (zhang_lili@ices.a-star.edu.sg) or Q.L. (qingliu@cqu.edu.cn)

Self-Assembly of Mesoporous Nanotubes Assembled from Interwoven Ultrathin Birnessite-type MnO_2 Nanosheets for Asymmetric Supercapacitors

Ming Huang[1], Yuxin Zhang[1,2], Fei Li[1], Lili Zhang[3], Rodney S. Ruoff[4], Zhiyu Wen[2] & Qing Liu[1]

[1]College of Materials Science and Engineering, Chongqing University, Chongqing 400044, P.R. China, [2]National Key Laboratory of Fundamental Science of Micro/Nano-Devices and System Technology, Chongqing University, Chongqing 400044, P.R. China, [3]Institute of Chemical and Engineering Sciences, A*STAR, 1 Pesek Road, Jurong Island 627833, Singapore, [4]Department of Mechanical Engineering and the Materials Science and Engineering Program, The University of Texas at Austin, One University Station C2200, Austin, Texas 78712, United States.

Porous nanotubes comprised of MnO_2 nanosheets were fabricated with a one-pot hydrothermal method using polycarbonate membrane as the template. The diameter and thickness of nanotubes can be controlled by choice of the membrane pore size and the chemistry. The porous MnO_2 nanotubes were used as a supercapacitor electrode. The specific capacitance in a three-electrode system was 365 F g^{-1} at a current density of 0.25 A g^{-1} with capacitance retention of 90.4% after 3000 cycles. An asymmetric supercapacitor with porous MnO_2 nanotubes as the positive electrode and activated graphene as the negative electrode yielded an energy density of 22.5 Wh kg^{-1} and a maximum power density of 146.2 kW kg^{-1}; these values exceeded those reported for other MnO_2 nanostructures. The supercapacitor performance was correlated with the hierarchical structure of the porous MnO_2 nanotubes.

With increasing demand for sustainable and renewable power sources in modern electronic industries, supercapacitors have attracted tremendous attention because of their high power density, excellent pulse charge-discharge characteristics, long cycling life and safe operation[1–3]. Up to now, various materials, including carbonaceous materials[4,5], conducting polymers[6], transition metal oxides/hydroxides[7,8], and hybrid composites[9,10], have been widely investigated as electrodes for supercapacitors. Compared to carbonaceous materials and conducting polymers, transition-metal oxides exhibit larger electrochemical capacitances and energy densities as they can provide a variety of oxidation states for efficient redox charge transfer which could satisfy the needs of high-performance supercapacitors. Hence, there has been extensive interest in developing the attractive transition metal oxide (such as MnO_2[11], Co_3O_4[12], NiO[13], VO_x[14], and CuO[15]) for supercapacitors.

In particular, manganese dioxide (MnO_2) has been extensively investigated as a supercapacitor electrode material due to its low cost, high natural abundance, high theoretical capacity (~1370 F g^{-1}), and non-toxicity[11,16–20]. The electrochemical performance of MnO_2 has been found to be strongly influenced by a variety of factors including preparation conditions, particle size, morphology, and degree of crystallinity, and others. While nanosheets[21,22], hollow spheres[23], nanoflowers[24], nanowires/nanorods[25–27], thin films[28,29], and nanotubes[30–32] have all been reported, the synthesis of MnO_2 with controllable particle size, morphology, and high crystallinity remained as a challenge. Among these structures, MnO_2 nanotubes can provide high surface area and a large surface-to-volume ratio to allow effective contact with the electrolyte ions, affording short ion diffusion paths and fast kinetics. The nanotube morphology can also accommodate large volume changes during the charge-discharge cycle and thereby improve the life of the electrode[33,34]. Although significant research has been devoted to the synthesis of MnO_2 nanotubes, there was no effective method for the production of porous MnO_2 nanotubes with precise morphological control. Dong et al.[35] reported the synthesis of porous MnO_2/TiN nanotube coaxial arrays *via* a two-step procedure based on an electrodeposition process, while elegant, the process is also complicated and tedious. Zhu et al. prepared the porous MnO_2 nanotubes using a hydrothermal method coupled with post-treatment. But the thickness of the MnO_2 wall and the diameter of the nanotube are difficult to control[36]. This motivated us to search for a simple way to prepare porous MnO_2 nanotube with controllable morphology.

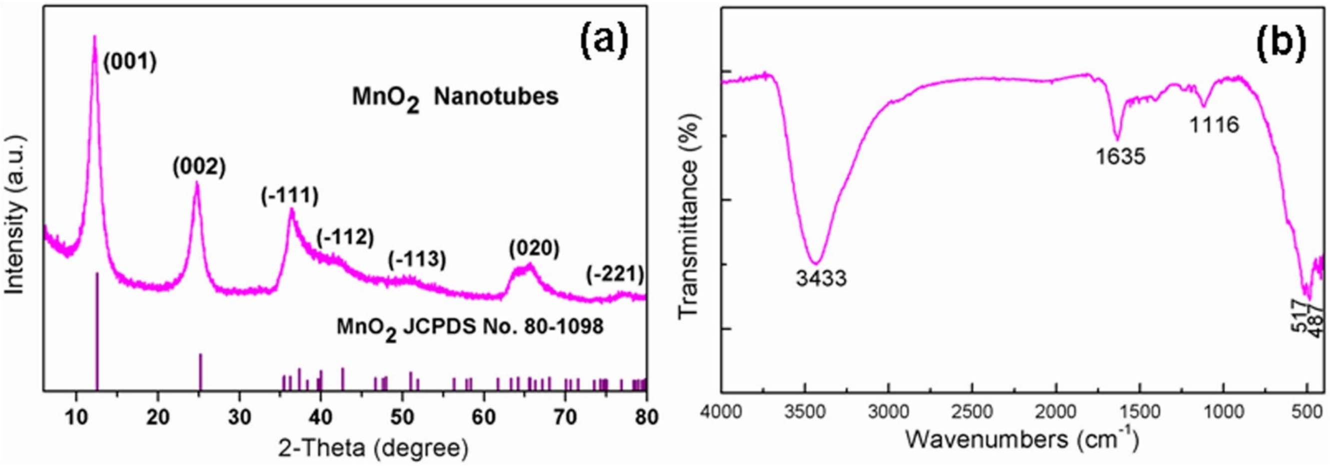

Figure 1 | (a) XRD pattern of nanotubes comprised of MnO_2 nanosheets. (b) FT-IR spectra of MnO_2 nanotubes.

In this work, we introduce a novel and effective one-step hydrothermal approach for the synthesis of porous MnO_2 nanotubes. The as-prepared MnO_2 nanotubes were porous and consisted of MnO_2 nanosheets with thickness of about 6 nm. The interconnected MnO_2 nanosheets in a mesoporous tubular structure can facilitate ion insertion/extraction and electron transport in the electrodes. An asymmetric supercapacitor with these porous MnO_2 nanotubes as the positive electrode and activated graphene as the negative electrode in 1 M Na_2SO_4 electrolyte had an energy density of 22.5 Wh kg^{-1} with a maximum power density of 146.2 kW kg^{-1}.

Results

The morphology of MnO_2 nanotubes can be tailored by varying the pore size of the polycarbonate (PC) membrane, the concentration of Mn precursors, the processing temperature and the time. PC membranes with pore size of 200 nm, and a processing temperature of 140°C were investigated in this study (Figs. S1 and S2 showed the SEM images of the PC membrane). The structure and phase purity of the as-prepared MnO_2 samples were examined by X-ray powder diffraction (XRD, Figure 1a). The diffraction peaks at about 12.5°, 25.2° and 37° from the as-prepared 200-nm diameter MnO_2 nanotubes matched the standard XRD pattern of birnessite-type manganese oxide crystal (JCPDS 80-1098, $a = 5.149$ Å, $b = 2.843$ Å, $c = 7.716$ Å). No other peaks that would be associated with another phase or impurity were observed. Fourier transform infrared spectroscopy (FT-IR) was used to characterize the functionality of MnO_2 nanotubes and the results were shown in Figure 1b. The main absorption bands were found at 3433, 1635, 1116, 517, and 487 cm^{-1}, respectively. The broad band around 3433 cm^{-1} represented the O-H stretching of the interlayer water molecules, while the weak band at 1635 cm^{-1} was probably due to the bending vibrations of the O-H groups from the adsorbed water molecules[37,38]. The absorption peak at 1116 cm^{-1} was attributed to the –OH bending vibrations combined with Mn atoms. The peaks at 517 and 487 cm^{-1} were the main characteristic absorption bands of birnessite, corresponding to Mn-O stretching modes of the octahedral layers in the birnessite structure which was consistent with the previous XRD result.

An illustration of the formation of MnO_2 nanotubes was shown in Figure 2a. The MnO_2 nuclei were firstly formed in a short time and adsorbed on the surface of the polycarbonate[39]. As the hydrothermal reaction further proceeded, Ostwald ripening process[40] took place, in which the smaller particles were consumed while the bigger ones grew into nanosheets with a lamellar structure[41,42]. Subsequently, the nanosheets were self-assembled into porous MnO_2 nanotubes

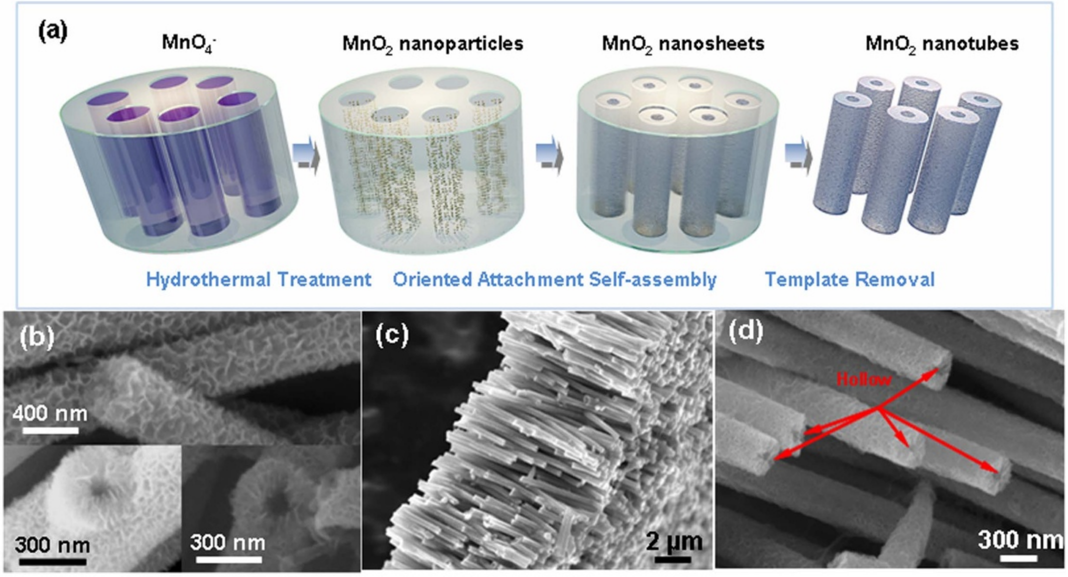

Figure 2 | (a) Schematic illustration of the procedure to synthesize porous MnO_2 nanotubes. SEM images of MnO_2 nanotubes. (b) Detailed images of the MnO_2 nanotubes. (c) Side-view of MnO_2 nanotubes arrays. (d) Enlarged view of the MnO_2 nanotubes arrays.

due to the "oriented attachment" and "self-assembly" processes[40], which involved a spontaneous self-organization[43,44] of the adjacent nanosheets.

Scanning electron microscope (SEM) images (Figure 2b–2d; see also Fig. S3) revealed that the average diameter of the MnO_2 nanotubes was about 200 nm, which is coincided with the average pore diameter of the original polycarbonate (PC) membrane. However, the length of the MnO_2 nanotubes ranged from 4 to 8 μm, which was shorter than the thickness of the PC membrane (Fig. S2). The length of the MnO_2 nanotubes was not uniform due to the fracture during the removal of the PC template. All the nanotubes were made of MnO_2 nanosheets. Each nanotube had flaky appearance, and the assembly of ultrathin nanosheets into interconnected porous structure provided large and open active area. The porous and hollow nanotubes were further elucidated by Transmission electron microscopy (TEM, Figure 3). High-resolution TEM (HRTEM, Figure 3b and c) images of the nanosheets clearly showed that the birnessite-type MnO_2 nanostructures were crystallized with the interplanar distance of 0.253 and 0.212 nm, corresponding to the (200) and (−112) plane of the birnessite-type MnO_2, respectively[41,42,45]. The interplanar spacing of MnO_2 nanosheet is 0.7 nm, corresponds to the typical interplanar spacing of the (001) plane of birnessite-type MnO_2 that prefers forming two-dimensional flaky structures. The corresponding selected area electron diffraction (SAED) pattern of the nanosheet edge exhibited polycrystalline nature of birnessite-type MnO_2. The lattice fringes attributing to the (200), (−112), and (020) planes were clearly visible, in agreement with the XRD results. Nitrogen adsorption-desorption results (see Supplementary Fig. S3) indicated that the MnO_2 nanotubes had a Brunauer-Emmett-Teller (BET) surface area of 85.2 $m^2\ g^{-1}$ with a pore volume of 0.394 $cm^3\ g^{-1}$. The pore size distribution obtained from the adsorption branch by the Barrett-Joyner-Halenda (BJH) method indicated that the average pore size was ~18 nm. The mesopore-in-nanotubular hierarchical morphology with controlled porous structures were advantageous for enhancive electrochemical capacitors applications since large specific surface area and open mesoporous tubular structures provided effective active sites for the chemical reactions, shortened the ion diffusion paths and facilitated rapid ion transport.

To evaluate the potential applications as the electrode materials for supercapacitor, the electrochemical properties of mesoporous MnO_2 nanotubes were firstly studied in a three-electrode system in 1 M Na_2SO_4 and the results were shown in Figure 4. The almost symmetric rectangular shape of the CV curves (Figure 4a) and the near linear symmetric triangular charge-discharge plots (Figure 4b) showed reversible and capacitive behavior of the MnO_2 nanotubes-based electrode. The specific capacitance of the electrode was calculated from the galvanostatic discharge curve using the following equation:

$$C = \frac{I\Delta t}{m\Delta V}$$

where C ($F\ g^{-1}$) is the specific capacitance, I (A) is the constant discharge current, Δt (s) is the discharge time, ΔV (V) is the potential window, and m (g) is the mass of the active material in the electrode. The specific capacitance of the MnO_2 nanotubes was 365 $F\ g^{-1}$ at the current density of 0.25 $A\ g^{-1}$; this value exceeded many MnO_2 electrodes in previous reports (Table S1)[41,46–54]. The corresponding volumetric capacitance of the total electrode including the current collector (Ni foam) was estimated to be about 107.4 ± 3 $F\ cm^{-3}$ according to the thickness (68 ± 2 μm) of the compressed MnO_2/Ni foam electrode. Furthermore, we have measured the electrochemical properties of two reference samples (commercial MnO_2 and MnO_2 nanosheets obtained without PC template) for comparison (Fig. S5). According to the discharge time from the charge/discharge curves (Fig. S5d), the as-prepared MnO_2 nanotubes show a much higher specific capacitance than the commercial MnO_2 (14.3 $F\ g^{-1}$) and MnO_2 nanosheets (194.5 $F\ g^{-1}$). The results show that the MnO_2 nanotubes are a promising candidate for the electrode materials for supercapacitors. The enhanced capacitive performance can be attributed to 1) the hierarchical-mesoporous nanotubular structure facilitated the ion insertion/extraction; and 2) the interconnected porous ultrathin MnO_2 nanosheets cannot only shorten the ion diffusion paths, but also ensure a high utilization of the active materials (since the redox reaction was surface reaction only and the bulk metal oxide did not contribute). The specific capacitance of MnO_2 nanotubes electrode at various current densities was shown in Figure 4c. When the current density was increased from 0.25 to 10 $A\ g^{-1}$, the specific capacitance can still be as high as 202.7 $F\ g^{-1}$ (decreased about 45%), indicating the good rate capability of the MnO_2 nanotubes.

The Nyquist plots of MnO_2 nanotubes electrode before and after 3000 cycles were obtained using AC electrochemical impedance spectroscopy (EIS) in the frequency range from 100 kHz to 0.01 Hz at open circuit potential by applying an AC voltage with 5 mV amplitude. The Nyquist plots in Figure 4d were composed of one semicircle in the high-frequency region and a linear part in the low-frequency region, which illustrated typical capacitor behavior. The contact resistances of the MnO_2 electrodes (before and after 3000 cycles) were 1.6 and 2.0 Ω, respectively, indicating good conductivity of the electrolyte and assembly of the cell. The equivalent circuit for the Nyquist plots was shown as an inset in Figure 4c (see Supplementary Table S2 for simulation result). After 3000 cycles, only a slight increase of the charge transfer resistance (Rct) from 3.9 to 7.4 Ω was observed.

Figure 4e showed the long-term cycling performance of the MnO_2 electrode by galvanostatic charge-discharge process at the current density of 5 $A\ g^{-1}$ for consecutive 3000 cycles. The specific capacitance

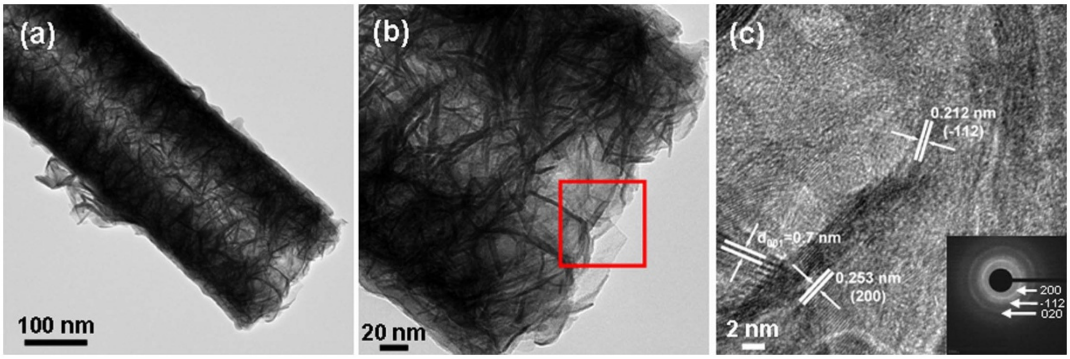

Figure 3 | (a) Low-magnification TEM image of an individual porous MnO_2 nanotube. (b) Detailed images of the terminal nanosheets of the MnO_2 nanotube. (c) HRTEM image of the MnO_2 nanosheets (the red boxed region in (b)). Bottom-right inset is the corresponding SAED pattern.

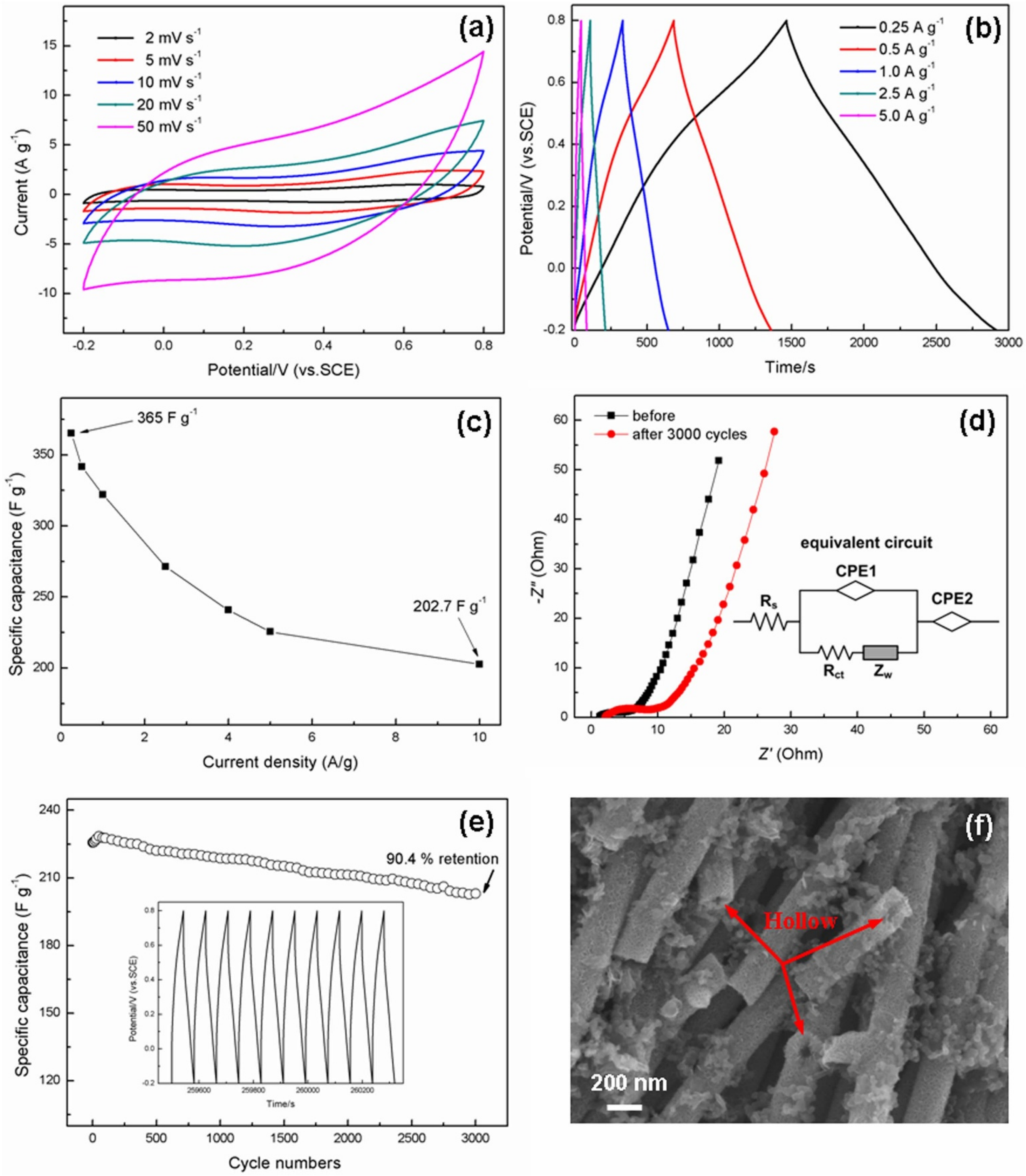

Figure 4 | (a) Cyclic voltammograms of MnO_2 nanotubes in a 1 M Na_2SO_4 aqueous electrolyte. (b) Charge-discharge curves of MnO_2 nanotubes at different current densities. (c) Specific capacitance of MnO_2 nanotubes measured under different current densities. (d) Electrochemical impedance spectrum of the MnO_2 nanotubes electrodes at open circuit potential in the frequency range from 0.01 Hz to 100 kHz. The inset shows the equivalent circuit. (e) Cycling performance of MnO_2 nanotubes at the current density of 5 $A\,g^{-1}$. The inset shows the charge-discharge curves of the last 10 cycles of the MnO_2 nanotubes electrode. (f) The corresponding SEM image of the electrode after 3000 electrochemical cycles.

of the MnO_2 nanotube-based electrode maintained about 90.4% of its initial value after 3000 cycles, demonstrating the good stability of the MnO_2 nanotubes as a supercapacitor's electrode. In addition, the charge-discharge curves of the last 10 cycles were shown as the inset in Figure 4e. The similar symmetric triangular charge-discharge curves (as comparing to the initial curve) indicated no significant structural change of the MnO_2 nanotubes electrode during the charge/discharge processes. Meanwhile, the SEM images of the MnO_2 nanotubes electrode before and after 3000 cycles were investigated (see Supplementary Fig. S6). The SEM image of the MnO_2 nanotube electrode after electrochemical cycles in Figure 4f suggested that the hierarchical porous nanotube structure was maintained rather well. The unique porous hollow nanostructure may resolve the aggregation problem and can accommodate the volume expansion of the electrode materials during long-term cycles, which was beneficial for the structural stability of the MnO_2 electrodes. The crystalline structure change of the MnO_2 nanotubes electrode after charge/discharge cycles at the current density of 1 A g^{-1} was examined through XRD. As shown in Figure S7, the interplanar spacing of MnO_2 increases slightly after the charge process (diffraction peaks are at a smaller degree), and then decreases during the following discharge (diffraction peaks at higher degree). After 3000 cycles, the crystallinity of MnO_2 was relatively well maintained which can be ascribed to small structural expansion/contraction occurring during charge/discharge cycles. The XRD results further demonstrated the good stability of the MnO_2 nanotubes for high-performance supercapacitors.

An asymmetric supercapacitor was fabricated using the MnO_2 nanotubes as the positive electrode and the activated graphene (AG) as the negative electrode with 1.0 M Na_2SO_4 aqueous electrolyte (Figure 5a). The SEM images and the electrochemical properties of the AG were shown in Figure S8 and S9 (see Supplementary Information). In the design cell, the mass ratio of the positive electrode (0.7 mg) to the negative electrode (1.3 mg) was fixed at 0.5 on the basis of the specific capacitance values and the potential windows of the two materials. The asymmetric device exhibited capacitive behavior with nearly rectangular-shaped CV curves without obvious redox peaks with the operating voltage up to 2.0 V (Figure 5b). Figure 5c showed the typical CV curves of the asymmetric cell in the voltage window from 0 to 1.8 V at the scan rates of 5, 10, 20, 50 and 100 mV s^{-1}. The CV profile of the asymmetric cell remained relatively rectangular at a high scan rate of 100 mV s^{-1}, which demonstrated good charge/discharge properties and rate capability of the asymmetric supercapacitor.

Discussion

The galvanostatic charge-discharge curves at various current densities were shown in Figure 5d. It can be seen that the potentials of the charge-discharge lines are nearly proportional to the charge or discharge time, indicating a rapid I–V response, small equivalent series resistance (ESR) and ideal capacitive characteristics. The EIS results (see Supplementary Fig. S10) of the asymmetric supercapacitor before and after 10000 cycles test confirmed the relative small change in the ESR. From the slope of the discharge curve, the gravimetric capacitance (*Ct*) of the asymmetric supercapacitor was 50 F g^{-1} based on the total mass of active materials in the two electrodes at a current density of 0.25 A g^{-1}. A maximum gravimetric energy density and power density of 22.5 Wh kg^{-1} and 146.2 kW kg^{-1} were obtained (Figure 5e), respectively, based on the total weight of the electrodes (i.e. mass of $MnO_2 + AG$). The values are not only higher than most of the MnO_2-based supercapacitors[41,55–67] but also comparable to those MnO_2-based composite supercapacitors[68–70] (see Supplementary Table S3 for detailed comparison). According to the fascinating synergetic properties or multifunctionalities of components[71,72], we can design a smart hybrid architecture based on mesoporous MnO_2 nanotubes with conductive supports or other metal oxide/hydroxide, and further improve the energy density of the MnO_2 nanotubes-based supercapacitors. The asymmetric supercapacitor device achieved a volumetric energy density and power density of 7.2 Wh L^{-1} and 46.8 kW L^{-1}, respectively, based on the total electrode (i.e. mass of $MnO_2 + AG + Ni$ foam) density of 4.0 g cm^{-3} (Table S3). In addition, the performance of the fully packaged asymmetric cell was also estimated (Table S4). The packaged device showed a maximum practical gravimetric energy density of 1.2 Wh kg^{-1} (highest power density of 7.5 kW kg^{-1}) and volumetric energy density of 5.0 Wh L^{-1} (highest power density of 31.5 kW L^{-1}). We connected our prototype device to a red LED and successfully lighted it (Figure 5f). More importantly, the LED was on for about 120 seconds after being charged for 27 s at 1.8 V (see Supplementary Movie S1). The device retained 76.3% of its initial specific capacitance after 10000 cycles (see Supplementary Fig. S11 and S12). In addition, the SEM images of MnO_2 nanotubes-based electrode in the asymmetric supercapacitor device after 10000 cycles revealed that the hierarchical porous MnO_2 nanotubes structure was well maintained (see Supplementary Fig. S13). These results showed our MnO_2 nanotubes//AG asymmetric supercapacitor device is promising in practical applications.

In summary, hierarchical and porous MnO_2 nanotubes comprised of ultrathin nanosheets have been prepared by a one-step hydrothermal treatment using PC as the template. The unique mesopore-in-nanotubular structure facilitated fast ion transport and the ultrathin MnO_2 nanosheet shortens the ion diffusion paths and ensured high utilization of the active material. The specific capacitance of the MnO_2 nanotubes-based electrode was 365 F g^{-1} at a current density of 0.25 A g^{-1} with capacitance retention of 90.4% retention after 3000 cycles in a three-electrode cell system. An asymmetric supercapacitor based on MnO_2 nanotubes as the positive electrode and AG as the negative electrode in aqueous electrolyte in a fully packaged cell was fabricated. The device can be reversibly charged and discharged at an operation voltage of 1.8 V in 1.0 M Na_2SO_4 aqueous electrolyte, delivering an energy density of 22.5 Wh kg^{-1} and a maximum power density of 146.2 kW kg^{-1}. The results indicated that the mesoporous MnO_2 nanotube is a promising candidate in electrochemically stable supercapacitors for practical applications. Such unique nanosheets-built MnO_2 nanotubes might also be used in broad fields including dye wastewater treatment and gas sensors. Furthermore, the proposed synthetic methodology would open new opportunities of other transition metal oxides for high-performance supercapacitors.

Methods

Materials. All the chemical reagents were purchased from Alfa Aesar, which are of analytical purity and used without any further purification. The polycarbonate (PC) membrane filters (Whatman 110606; pore diameter: 200 nm) were used for the fabrication of mesoporous MnO_2 nanotubes.

Preparation of nanotubes comprised of MnO_2 nanosheets. Prior of being used, the PC substrate was treated by hydrochloric acid (1 M) to remove the impurities on the surface of PC. The MnO_2 nanotubes were prepared in $KMnO_4$ solution using the PC as the template. In a typical synthetic procedure, the treated PC membrane was immersed in $KMnO_4$ solution (0.02 M; 30 mL) under ultrasonication for 20 minutes. The mixture (including the PC membrane) was transferred into a Teflon-lined stainless steel autoclave which was subsequently maintained at 140°C for 24 h. The MnO_2/PC membrane composite was then taken out from the solution and dissolved away PC in dichloromethane to obtain pure MnO_2 sample. Finally, the MnO_2 sample was washed with distilled water and ethanol, and dried at 60°C to obtain the porous MnO_2 nanotubes.

Electrochemical measurements. A three-electrode system was used to measure the response of the MnO_2 nanotubes as the working electrode using 1 M Na_2SO_4 aqueous solution as the electrolyte, with a platinum plate as the counter electrode and saturated calomel electrode (SCE) as the reference electrode, respectively. The working electrode was prepared by mixing 70 wt% active material (MnO_2 nanotubes), 20 wt% acetylene black and 10 wt% polyvinylidene fluoride (PVDF) in N-methyl-2-pyrrolidone (NMP) and the slurry was spread onto a foam nickel current collector (1×1 cm^2). The electrode was heated at 120°C for 12 h to evaporate the solvent and then uniaxially pressed under 10 MPa. The electrode contained 2 mg of active materials (MnO_2 nanotubes alone).

The asymmetric supercapacitor was measured with a two-electrode system, including two slices of electrode material with the same size, a Whatman filter paper as separator, and two pieces of nickel foil as the current collectors. In the two-electrode system, MnO_2 nanotubes were the positive electrode, and activated graphene (AG) mixed with 20 wt% acetylene black and 10 wt% polyvinylidene fluoride (PVDF) in N-methyl-2-pyrrolidone (NMP) to form a paste and then pressed into uniform sheet was the negative electrode. The two electrodes were assembled together with Whatman filter paper soaked in 1 M Na_2SO_4 solution before being connected to the potentiostat. The electrochemical performance in both three-electrode and two-electrode configurations were carried out on the CHI 660E electrochemical station.

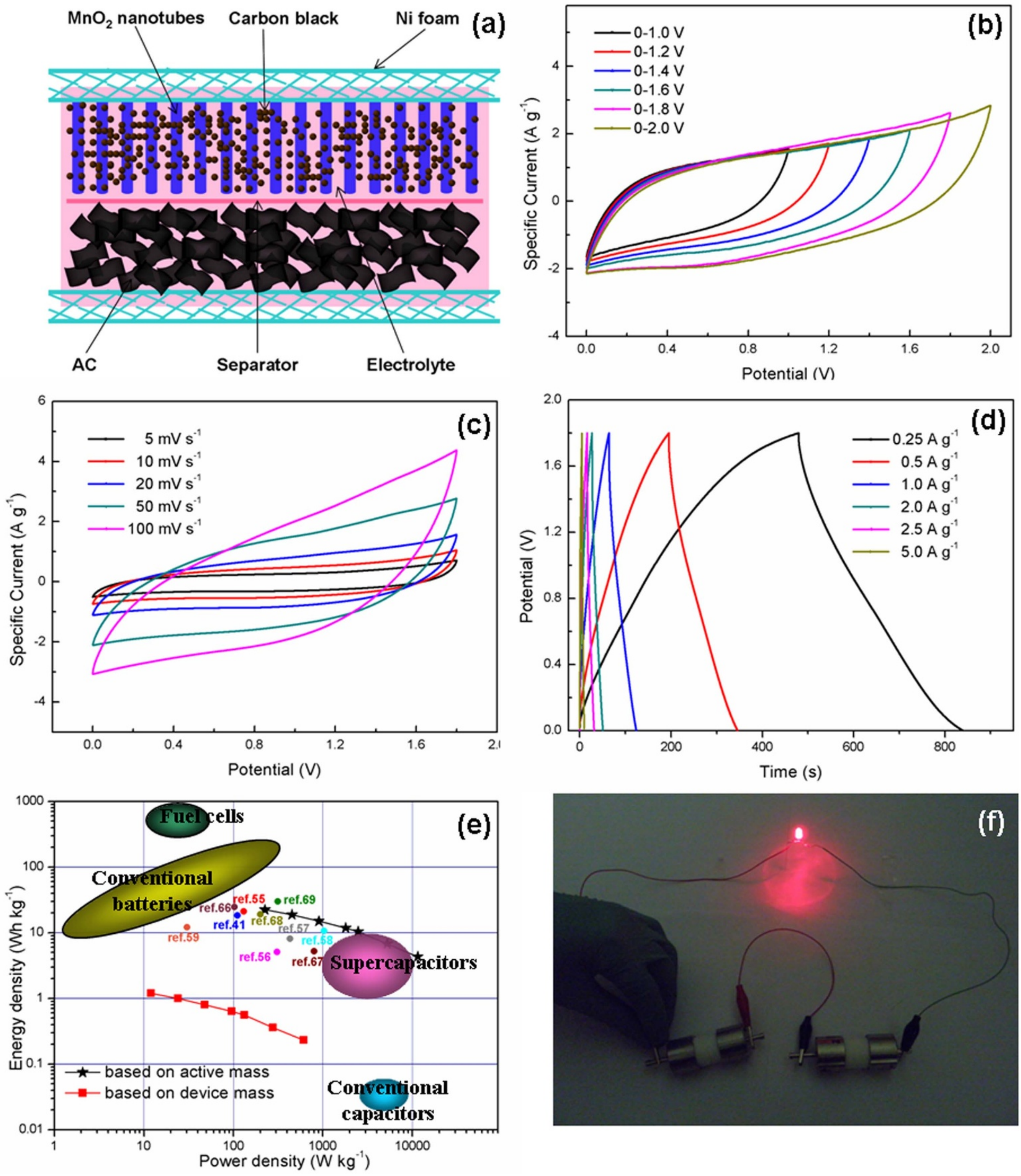

Figure 5 | (a) Schematic illustration of the asymmetric supercapacitor configuration. (b) CV curves of MnO_2 nanosheets-bulit nanotubes//AG asymmetric supercapacitor measured at different potential window at a scan rate of 50 mV s^{-1}. (c) CV curves of the asymmetric supercapacitor measured at different scan rates between 0 and 1.8 V. (d) Galvanostatic charge-discharge curves at different current densities. (e) The energy density *vs.* power density of the MnO_2 nanotubes//AG asymmetric supercapacitor in a Ragone plot for fuel cells, conventional batteries, conventional capacitors, and ultracapacitors. (f) Digital image of a red-light-emitting diode (LED) lighted by the MnO_2 nanotubes//AG device.

The cyclic voltammetry (CV) and galvanostatic charge-discharge techniques were employed to investigate the electrochemical performance of the electrodes. All the operating current densities were calculated based on the mass of active materials (mass of MnO_2 nanotubes for three-electrode system and the total weight of MnO_2 nanotubes with AG for two-electrode system). The electrochemical impedance spectroscopy (EIS) was conducted in the frequency range between 100 kHz and 0.01 Hz with a perturbation amplitude of 5 mV versus the open-circuit potential.

1. Miller, J. R. & Simon, P. Materials science - Electrochemical capacitors for energy management. *Science* **321**, 651–652 (2008).
2. Simon, P. & Gogotsi, Y. Materials for electrochemical capacitors. *Nat. Mater.* **7**, 845–854 (2008).
3. Liu, C., Li, F., Ma, L.-P. & Cheng, H.-M. Advanced materials for energy storage. *Adv. Mater.* **22**, E28–E62 (2010).
4. Chaikittisilp, W., Ariga, K. & Yamauchi, Y. A new family of carbon materials: synthesis of MOF-derived nanoporous carbons and their promising applications. *J. Mater. Chem. A* **1**, 14–19 (2013).
5. Chaikittisilp, W. *et al.* Nanoporous carbons through direct carbonization of a zeolitic imidazolate framework for supercapacitor electrodes. *Chem. Commun.* **48**, 7259–7261 (2012).
6. Ermis, E., Yigit, D. & Gullu, M. Synthesis of poly(N-alkyl-3,4-dihydrothieno 3,4-b 1,4 oxazine) derivatives and investigation of their supercapacitive performances for charge storage applications. *Electrochim. Acta* **90**, 623–633 (2013).
7. Hu, M., Ishihara, S. & Yamauchi, Y. Bottom-up synthesis of monodispersed single-crystalline cyano-bridged coordination polymer nanoflakes. *Angew. Chem. Int. Ed.* **52**, 1235–1239 (2013).
8. Ji, J. *et al.* Nanoporous $Ni(OH)_2$ thin film on 3D ultrathin-graphite foam for asymmetric supercapacitor. *ACS Nano* **7**, 6237–6243 (2013).
9. Yang, Y. *et al.* Vapor phase polymerization deposition of conducting polymer/graphene nanocomposites as high performance electrode materials. *ACS Appl. Mater. Interfaces* **5**, 4350–4355 (2013).
10. Bastakoti, B. P. *et al.* Mesoporous carbon incorporated with In_2O_3 nanoparticles as high-performance supercapacitors. *Eur. J. Inorg. Chem.* **2013**, 1109–1112 (2013).
11. Zhao, X. *et al.* Incorporation of manganese dioxide within ultraporous activated graphene for high-performance electrochemical capacitors. *ACS Nano* **6**, 5404–5412 (2012).
12. Xia, X.-H., Tu, J.-P., Wang, X.-L., Gu, C.-D. & Zhao, X.-B. Mesoporous Co_3O_4 monolayer hollow-sphere array as electrochemical pseudocapacitor material. *Chem. Commun.* **47**, 5786–5788 (2011).
13. Zhang, Y. Q. *et al.* Self-assembled synthesis of hierarchically porous NiO film and its application for electrochemical capacitors. *J. Power Sources* **199**, 413–417 (2012).
14. Qu, Q., Zhu, Y., Gao, X. & Wu, Y. Core-shell structure of polypyrrole grown on V_2O_5 nanoribbon as high performance anode material for supercapacitors. *Adv. Energy Mater.* **2**, 950–955 (2012).
15. Dubal, D. P., Gund, G. S., Holze, R. & Lokhande, C. D. Mild chemical strategy to grow micro-roses and micro-woolen like arranged CuO nanosheets for high performance supercapacitors. *J. Power Sources* **242**, 687–698 (2013).
16. Wei, W., Cui, X., Chen, W. & Ivey, D. G. Manganese oxide-based materials as electrochemical supercapacitor electrodes. *Chem. Soc. Rev.* **40**, 1697–1721 (2011).
17. Li, Q. *et al.* Design and synthesis of MnO_2/Mn/MnO_2 sandwich-structured nanotube arrays with high supercapacitive performance for electrochemical energy storage. *Nano Lett.* **12**, 3803–3807 (2012).
18. Chen, K., Noh, Y. D., Li, K., Komarneni, S. & Xue, D. Microwave-hydrothermal crystallization of polymorphic MnO_2 for electrochemical energy storage. *J. Phys. Chem. C* **117**, 10770–10779 (2013).
19. Kang, J. *et al.* Enhanced supercapacitor performance of MnO_2 by atomic doping. *Angew. Chem. Int. Ed.* **52**, 1664–1667 (2013).
20. Zhang, Y. X., Huang, M., Li, F., Wang, X. L. & Wen, Z. Q. One-pot synthesis of hierarchical MnO_2-modified diatomites for electrochemical capacitor electrodes. *J. Power Sources* **246**, 449–456 (2014).
21. Zhang, Y. *et al.* Crystallization design of MnO_2 towards better supercapacitance. *CrystEngComm* **14**, 5892–5897 (2012).
22. Kai, K. *et al.* Electrochemical characterization of single-layer MnO_2 nanosheets as a high-capacitance pseudocapacitor electrode. *J. Mater. Chem.* **22**, 14691–14695 (2012).
23. Tang, X., Liu, Z.-h., Zhang, C., Yang, Z. & Wang, Z. Synthesis and capacitive property of hierarchical hollow manganese oxide nanospheres with large specific surface area. *J. Power Sources* **193**, 939–943 (2009).
24. Su, M. *et al.* Three-dimensional nanoflower-like MnO_2 functionalized graphene as catalytically promoted nanolabels for ultrasensitive electrochemiluminescence immunoassay. *Electrochim. Acta* **97**, 333–340 (2013).
25. Wei, C. *et al.* Two-dimensional beta-MnO_2 nanowire network with enhanced electrochemical capacitance. *Sci. Rep.* **3**, 2193 (2013).
26. Yu, M. *et al.* Manganese dioxide nanorod arrays on carbon fabric for flexible solid-state supercapacitors. *J. Power Sources* **239**, 64–71 (2013).
27. Lu, X. *et al.* Facile synthesis of large-area manganese oxide nanorod arrays as a high-performance electrochemical supercapacitor. *Energy Environ. Sci.* **4**, 2915–2921 (2011).
28. Yan, D. *et al.* MnO_2 film with three-dimensional structure prepared by hydrothermal process for supercapacitor. *J. Power Sources* **199**, 409–412 (2012).
29. Yang, D. Pulsed laser deposition of manganese oxide thin films for supercapacitor applications. *J. Power Sources* **196**, 8843–8849 (2011).
30. Xiao, W., Xia, H., Fuh, J. Y. H. & Lu, L. Growth of single-crystal alpha-MnO_2 nanotubes prepared by a hydrothermal route and their electrochemical properties. *J. Power Sources* **193**, 935–938 (2009).
31. Li, L., Nan, C., Lu, J., Peng, Q. & Li, Y. Alpha-MnO_2 nanotubes: high surface area and enhanced lithium battery properties. *Chem. Commun.* **48**, 6945–6947 (2012).
32. Luo, J. *et al.* Synthesis of single-crystal tetragonal alpha-MnO_2 nanotubes. *J. Phys. Chem. C* **112**, 12594–12598 (2008).
33. Yan, W. *et al.* Mesoporous manganese oxide nanowires for high-capacity, high-rate, hybrid electrical energy storage. *ACS Nano* **5**, 8275–8287 (2011).
34. Chen, S., Zhu, J., Wu, X., Han, Q. & Wang, X. Graphene oxide-MnO_2 nanocomposites for supercapacitors. *ACS Nano* **4**, 2822–2830 (2010).
35. Dong, S. *et al.* One dimensional MnO_2/titanium nitride nanotube coaxial arrays for high performance electrochemical capacitive energy storage. *Energy Environ. Sci.* **4**, 3502–3508 (2011).
36. Zhu, J. *et al.* Oxidation-etching preparation of MnO_2 tubular nanostructures for high-performance supercapacitors. *ACS Appl. Mater. Interfaces* **4**, 2769–2774 (2012).
37. Yao, W., Zhou, H. & Lu, Y. Synthesis and property of novel MnO_2@polypyrrole coaxial nanotubes as electrode material for supercapacitors. *J. Power Sources* **241**, 359–366 (2013).
38. Huang, Y., Lin, Y. & Li, W. Controllable syntheses of alpha- and delta-MnO_2 as cathode catalysts for zinc-air battery. *Electrochim. Acta* **99**, 161–165 (2013).
39. Bechelany, M., Amin, A., Brioude, A., Cornu, D. & Miele, P. ZnO nanotubes by template-assisted sol–gel route. *J. Nanopart. Res.* **14**, 1–7 (2012).
40. Zeng, H. C. Ostwald ripening: A synthetic approach for hollow nanomaterials. *Curr. Nanosci.* **3**, 177–181 (2007).
41. Zhang, X. *et al.* Rapid hydrothermal synthesis of hierarchical nanostructures assembled from ultrathin birnessite-type MnO_2 nanosheets for supercapacitor applications. *Electrochim. Acta* **89**, 523–529 (2013).
42. Zhou, J. *et al.* Novel synthesis of birnessite-type MnO_2 nanostructure for water treatment and electrochemical capacitor. *Ind. Eng. Chem. Res.* **52**, 9586–9593 (2013).
43. Fang, X. S. *et al.* Direct observation of the growth process of MgO nanoflowers by a simple chemical route. *Small* **1**, 422–428 (2005).
44. Wang, F. *et al.* Manganese oxides with rod-, wire-, tube-, and flower-like morphologies: highly effective catalysts for the removal of toluene. *Environ. Sci. Technol.* **46**, 4034–4041 (2012).
45. Liu, J. *et al.* Co_3O_4 nanowire@MnO_2 ultrathin nanosheet core/shell arrays: a new class of high-performance pseudocapacitive materials. *Adv. Mater.* **23**, 2076–2081 (2011).
46. Yeager, M. *et al.* Highly efficient $K_{0.15}MnO_2$ birnessite nanosheets for stable pseudocapacitive cathodes. *J. Phys. Chem. C* **116**, 20173–20181 (2012).
47. Ming, B. *et al.* Microwave-hydrothermal synthesis of birnessite-type MnO_2 nanospheres as supercapacitor electrode materials. *J. Power Sources* **198**, 428–431 (2012).
48. Dubal, D. P., Dhawale, D. S., Salunkhe, R. R. & Lokhande, C. D. A novel chemical synthesis of Mn_3O_4 thin film and its stepwise conversion into birnessite MnO_2 during super capacitive studies. *J. Electroanal. Chem.* **647**, 60–65 (2010).
49. Munaiah, Y., Raj, B. G. S., Kumar, T. P. & Ragupathy, P. Facile synthesis of hollow sphere amorphous MnO_2: the formation mechanism, morphology and effect of a bivalent cation-containing electrolyte on its supercapacitive behavior. *J. Mater. Chem. A* **1**, 4300–4306 (2013).
50. Kundu, M. & Liu, L. Direct growth of mesoporous MnO_2 nanosheet arrays on nickel foam current collectors for high-performance pseudocapacitors. *J. Power Sources* **243**, 676–681 (2013).
51. Sopcic, S., Peter, R., Petravic, M. & Mandic, Z. New insights into the mechanism of pseudocapacitance deterioration in electrodeposited MnO_2 under negative potentials. *J. Power Sources* **240**, 252–257 (2013).
52. Song, Z. *et al.* A facile template-free synthesis of alpha-MnO_2 nanorods for supercapacitor. *J. Alloys Compd.* **560**, 151–155 (2013).
53. Li, W. *et al.* MnO_2 ultralong nanowires with better electrical conductivity and enhanced supercapacitor performances. *J. Mater. Chem.* **22**, 14864–14867 (2012).
54. Xia, H., Feng, J., Wang, H., Lai, M. O. & Lu, L. MnO_2 nanotube and nanowire arrays by electrochemical deposition for supercapacitors. *J. Power Sources* **195**, 4410–4413 (2010).
55. Qu, Q. T. *et al.* A new cheap asymmetric aqueous supercapacitor: activated carbon//$NaMnO_2$. *J. Power Sources* **194**, 1222–1225 (2009).
56. He, Y. *et al.* Freestanding three-dimensional graphene/MnO_2 composite networks as ultra light and flexible supercapacitor electrodes. *ACS Nano* **7**, 174–182 (2013).
57. Cottineau, T., Toupin, M., Delahaye, T., Brousse, T. & Belanger, D. Nanostructured transition metal oxides for aqueous hybrid electrochemical supercapacitors. *Appl. Phys. A* **82**, 599–606 (2006).
58. Chen, C.-Y., Fan, C.-Y., Lee, M.-T. & Chang, J.-K. Tightly connected MnO_2–graphene with tunable energy density and power density for supercapacitor applications. *J. Mater. Chem.* **22**, 7697–7700 (2012).
59. Bahloul, A. *et al.* Polypyrrole-covered MnO_2 as electrode material for supercapacitor. *J. Power Sources* **240**, 267–272 (2013).
60. Yu, G. *et al.* Solution-processed graphene/MnO_2 nanostructured textiles for high-performance electrochemical capacitors. *Nano Lett.* **11**, 2905–2911 (2011).
61. Jaidev, Jafri, R. I., Mishra, A. K. & Ramaprabhu, S. Polyaniline–MnO_2 nanotube hybrid nanocomposite as supercapacitor electrode material in acidic electrolyte. *J. Mater. Chem.* **21**, 17601–17605 (2011).
62. Deng, L. *et al.* Graphene-MnO_2 and graphene asymmetrical electrochemical capacitor with a high energy density in aqueous electrolyte. *J. Power Sources* **196**, 10782–10787 (2011).

63. Sun, Z., Firdoz, S., Yap, E. Y.-X., Li, L. & Lu, X. Hierarchically structured MnO_2 nanowires supported on hollow Ni dendrites for high-performance supercapacitors. *Nanoscale* **5**, 4379–4387 (2013).
64. Wu, T.-H., Chu, Y.-H., Hu, C.-C. & Hardwick, L. J. Criteria appointing the highest acceptable cell voltage of asymmetric supercapacitors. *Electrochem. Commun.* **27**, 81–84 (2013).
65. Xu, C., Du, H., Li, B., Kang, F. & Zeng, Y. Asymmetric activated carbon-manganese dioxide capacitors in mild aqueous electrolytes containing alkaline-earth cations. *J. Electrochem. Soc.* **156**, A435–A441 (2009).
66. Lei, Z., Zhang, J. & Zhao, X. S. Ultrathin MnO_2 nanofibers grown on graphitic carbon spheres as high-performance asymmetric supercapacitor electrodes. *J. Mater. Chem.* **22**, 153–160 (2012).
67. Wang, Y.-S., Tsai, D.-S., Chung, W.-H., Syu, Y.-S. & Huang, Y.-S. Power loss and energy density of the asymmetric ultracapacitor loaded with molybdenum doped manganese oxide. *Electrochim. Acta* **68**, 95–102 (2012).
68. Wu, Z.-S. *et al.* High-energy MnO_2 nanowire/graphene and graphene asymmetric electrochemical capacitors. *ACS Nano* **4**, 5835–5842 (2010).
69. Fan, Z. *et al.* Asymmetric supercapacitors based on graphene/MnO_2 and activated carbon nanofiber electrodes with high power and energy density. *Adv. Funct. Mater.* **21**, 2366–2375 (2011).
70. Gao, H., Xiao, F., Ching, C. B. & Duan, H. High-performance asymmetric supercapacitor based on graphene hydrogel and nanostructured MnO_2. *ACS Appl. Mater. Interfaces* **4**, 2801–2810 (2012).
71. Chen, H. *et al.* One-step fabrication of ultrathin porous nickel hydroxide-manganese dioxide hybrid nanosheets for supercapacitor electrodes with excellent capacitive performance. *Adv. Energy Mater.* (2013) DOI: 10.1002/aenm.201300580.
72. Chen, H., Zhou, S., Chen, M. & Wu, L. Reduced graphene oxide–MnO_2 hollow sphere hybrid nanostructures as high-performance electrochemical capacitors. *J. Mater. Chem.* **22**, 25207–25216 (2012).

Acknowledgments

The authors gratefully acknowledge the financial supports provided by National Natural Science Foundation of China (Grant no. 51104194), Doctoral Fund of Ministry of Education of China (20110191120014), No. 43 Scientific Research Foundation for the Returned Overseas Chinese Scholars, National Key laboratory of Fundamental Science of Micro/Nano-device and System Technology (2013MS06, Chongqing University), State Education Ministry and Fundamental Research Funds for the Central Universities (Project no. CDJZR12248801, CDJZR12135501, and CDJZR13130035, Chongqing University, PR China).

Author contributions

Y.X.Z., L.L.Z. and Q.L. conceived and designed the experiments. M.H. and F.L. prepared self-assembled nanostructures and the supercapacitor electrodes, and conducted the electrochemical measurements. Z.Y.W. helped with TEM and electrochemical measurements and initial studies. R.S.R. helped with modification of manuscripts and kind discussion on details. Y.X.Z., Z.Y.W. and Q.L. wrote the manuscript. All the authors commented on the manuscript.

Additional information

Supplementary information accompanies this paper at http://www.nature.com/scientificreports

Competing financial interests: The authors declare no competing financial interests.

How to cite this article: Huang, M. *et al.* Self-Assembly of Mesoporous Nanotubes Assembled from Interwoven Ultrathin Birnessite-type MnO_2 Nanosheets for Asymmetric Supercapacitors. *Sci. Rep.* **4**, 3878; DOI:10.1038/srep03878 (2014).